

Article

Geology, Geochemistry, and Geochronology of Gabbro from the Haoyaoerhudong Gold Deposit, Northern Margin of the North China Craton

Jianping Wang *, Xiu Wang, Jiajun Liu, Zhenjiang Liu, Degao Zhai and Yinhong Wang

School of Earth Sciences and Resources, China University of Geosciences, Beijing 100083, China; wangxiucugb@163.com (X.W.); liujiajun@cugb.edu.cn (J.L.); lzj@cugb.edu.cn (Z.L.); dgzhai@cugb.edu.cn (D.Z.); wyh@cugb.edu.cn (Y.W.)

* Correspondence: jpwang@cugb.edu.cn; Tel.: +86-10-8232-2264

Received: 5 December 2018; Accepted: 17 January 2019; Published: 21 January 2019



Abstract: The Haoyaoerhudong gabbro is a mafic intrusion located in the Haoyaoerhudong gold deposit, which is a giant gold deposit (148 t Au) hosted in Proterozoic strata on the northern margin of the North China Craton. In this paper, we present integrated SHRIMP U–Pb, geochemical and Sr–Nd isotopic data from gabbro of the Haoyaoerhudong gold deposit to reveal the magmatic processes behind its origin. SHRIMP zircon U–Pb dating constrains the timing of crystallization of the Haoyaoerhudong gabbro to 278.8 ± 0.81 Ma. Whole-rock geochemical results indicate that the Haoyaoerhudong gabbro has calc-alkaline features with enrichments of large-ion lithophile elements (LILE) and light rare-earth elements (REE) as well as depletions of high-field strength elements (HFSE). The relatively high ($^{87}\text{Sr}/^{86}\text{Sr}$)_i (0.7053 to 0.7078) and low $\epsilon\text{Nd}(t)$ (−4.6 to −15.1) values of the gabbro indicate the involvement of crustal materials. Low Ce/Pb ratios (1.35 to 7.38), together with nearly constant La/Sm and Th/Yb ratios and variable Ba/Th and Sr/Nd ratios, suggest that the ancient mantle was modified by slab dehydration fluids. Based on new geochemical data and regional geological investigations, we propose that both the Haoyaoerhudong gold deposit and the Haoyaoerhudong gabbro formed in a post-orogenic extensional setting.

Keywords: geochemistry; U–Pb zircon age; Sr–Nd isotopes; Haoyaoerhudong gabbro; Inner Mongolia

1. Introduction

The North China Craton (NCC) is a well-known Precambrian block in China [1–3]. The amalgamation between the eastern and western blocks ca. 1.85 Ga marked the cratonization process of the NCC [4]. Its northern margin underwent a strong rifting process, forming the Langshan–Zhaertaishan Rift and the Bayan Obo Rift during the Proterozoic era. Affected by the evolution of the Central Asian Orogenic Belt (CAOB), a giant magmatic rock belt formed along the northern margin of the NCC during the Paleozoic era (Figure 1) [5–8]. Several large orogenic gold deposits, including the Zhulazhaga and Haoyaoerhudong gold deposits, formed during the Paleozoic orogenic process.

The Haoyaoerhudong gold deposit is a super large (148 t Au) low-grade deposit in the western part of the NCC. Gold is hosted by pyrite and pyrrhotite, which were mainly deposited on bedding and schistosity planes of the Proterozoic black shales [9]. Hercynian intrusions are common in the Haoyaoerhudong gold district. A small gabbro intrusion is located west of the Haoyaoerhudong gold deposit (called the Haoyaoerhudong gabbro below). Most previous research focused on the gold deposit itself and the granitoids around the deposit [10–14], but little is known about the Haoyaoerhudong gabbro.

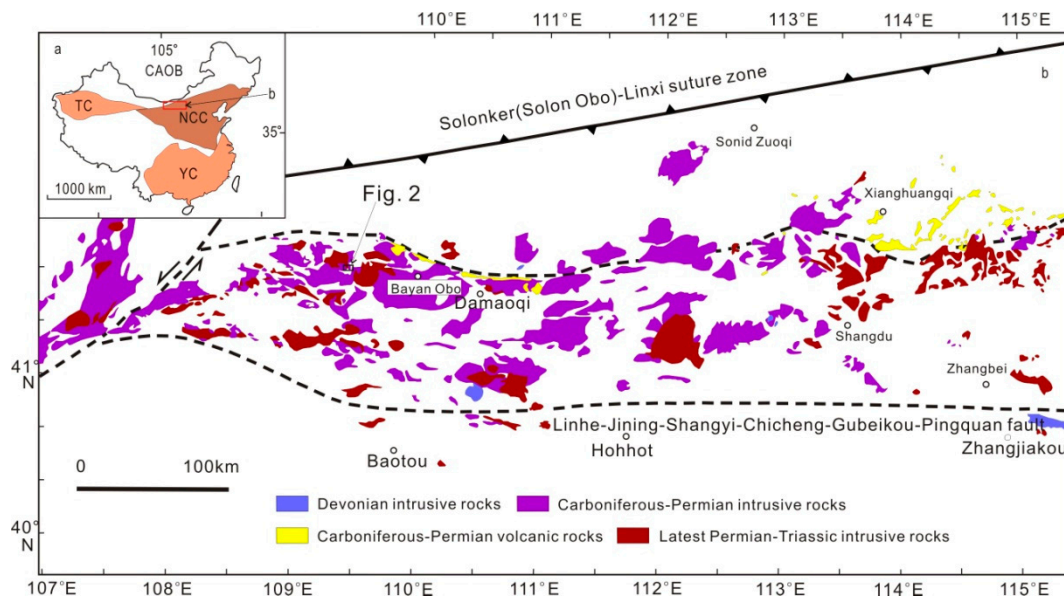


Figure 1. (a) Tectonic framework of China, showing the location of (b) Distribution of Paleozoic magmatic rocks along the northern margin of the North China Craton (NCC) (modified after [6]). TC, Tarim Craton; YC, Yangtze Craton.

Mafic rocks, although in a small volume on the earth's surface, are very important study subjects to explore deep mantle heterogeneity, crust-mantle interactions [15], and the tectonic properties of different blocks in ancient orogens [16]. The presence of the Haoyaoerhudong gabbro gives us an opportunity to investigate the composition of the ancient mantle, crust-mantle interaction, and crustal differentiation [17] of the northern margin of the NCC. We report new data of whole-rock geochemistry, zircon U–Pb dating, and Sr–Nd isotopes of the Haoyaoerhudong gabbro with the goal of constraining the petrogenesis and timing of the gabbro as well as the geodynamic setting of the Permian magmatism and related gold mineralization.

2. Geological Setting

A “double rift” system developed on the northern margin of the NCC in the Proterozoic era [18]. The Langshan–Zhaertaishan Rift (inside) and the Bayan Obo Rift (outside), host gigantic thick Proterozoic rift sediments called the Zhaertaishan and Bayan Obo Groups, respectively. The supracrustal succession of the Zhaertaishan and Bayan Obo Groups are thought to be contemporaneous with different types of magmatism [19–21]. Carbonates characterized the Bayan Obo Rift [22–24], whereas double-peak volcanism occurred in the Langshan–Zhaertaishan Rift [25]. The giant Bayan Obo REE–Nb–Fe deposit is located in the Bayan Obo Group, and the superlarge Langshan–Zhaertaishan SEDEX (sedimentary exhalative) Pb–Zn–Cu–S ore belt (including the Dongshengmiao, Huogeqi, Tanyaokou, and Jiashengpan ore deposits) is hosted in the Zhaertaishan Group. Carbonate dikes and bimodal magmatism indicate that the northern margin of the NCC experienced rifting in the Middle Mesoproterozoic, which is considered to be the result of the final breakup of the Columbia Supercontinent [21], and induced the formation of the Bayan Obo REE–Nb–Fe deposit and the giant Langshan–Zhaertaishan SEDEX ore belt. Along with the evolution of the CAOB, the northern margin of the NCC experienced an orogenic process with strong tectono-magmatism during the Paleozoic. Large volumes of magmatic rocks currently crop out along the northern margin of the NCC (Figure 1). Zhang et al. [6] summarized three important magmatic events: Devonian (from 400 to 360 Ma), late Early Carboniferous to Middle Permian (from 330 to 265 Ma), and latest Permian to Triassic (from 250 to 200 Ma). The most striking regional structure is the Solonker suture zone. This zone, which is composed of ophiolites and olistostromes, is thought to be the remnants

of the Paleo-Asian Ocean. Additional information about the regional tectonic evolution is given in references [2,26,27].

The geology of the Haoyaoerhudong gold deposit is similar to the northern margin of the NCC, which is characterized by Proterozoic strata divided by Paleozoic magmatic rocks. The Bayan Obo Group exposed in the gold district include the Jianshan, Halahuogete, and Bilute formations [9,14]. The Bilute Formation, which is mainly composed of black shales (rich in organic material, with an average TOC of 3.4%), is the major gold-hosting rock (Figure 2). Most intrusions are Permian in age, and the main lithologies include granitic porphyry, monzogranitic porphyry, granodiorite, and biotite granite. The granite porphyry and monzonitic granite porphyry have zircon U–Pb ages of 290.9 ± 2.8 Ma and 287.5 ± 1.9 Ma, respectively. The biotite granite samples yield zircon U–Pb ages of 267.9 ± 1.2 Ma and 274.0 ± 2.3 Ma [11,12]. Gold-related alteration ages are reported as 270.1 ± 2.5 Ma (biotite Ar–Ar [9]) and 250.9 ± 1.5 Ma (muscovite Ar–Ar [13]). Most researchers have inferred a genetic relation between the gold mineralization and the Permian tectono-magmatism [9,13,14,28].

The Haoyaoerhudong gabbro is located in the Haoyaoerhudong gold ore district, approximately 2 km southwest of the west open pit (Figure 2). It is an oval intrusion with an area of about 2.5 km². The gabbro mainly intrudes into the Halahuogete Formation, nearly parallel to the border between the Halahuogete Formation and the Bilute Formation to the north. The gabbro truncates the gray-white tonalite in the southwest area (Figure 2). Several NE-SW-trending gabbro dikes are present in the Haoyaoerhudong gold district (Figure 3A).

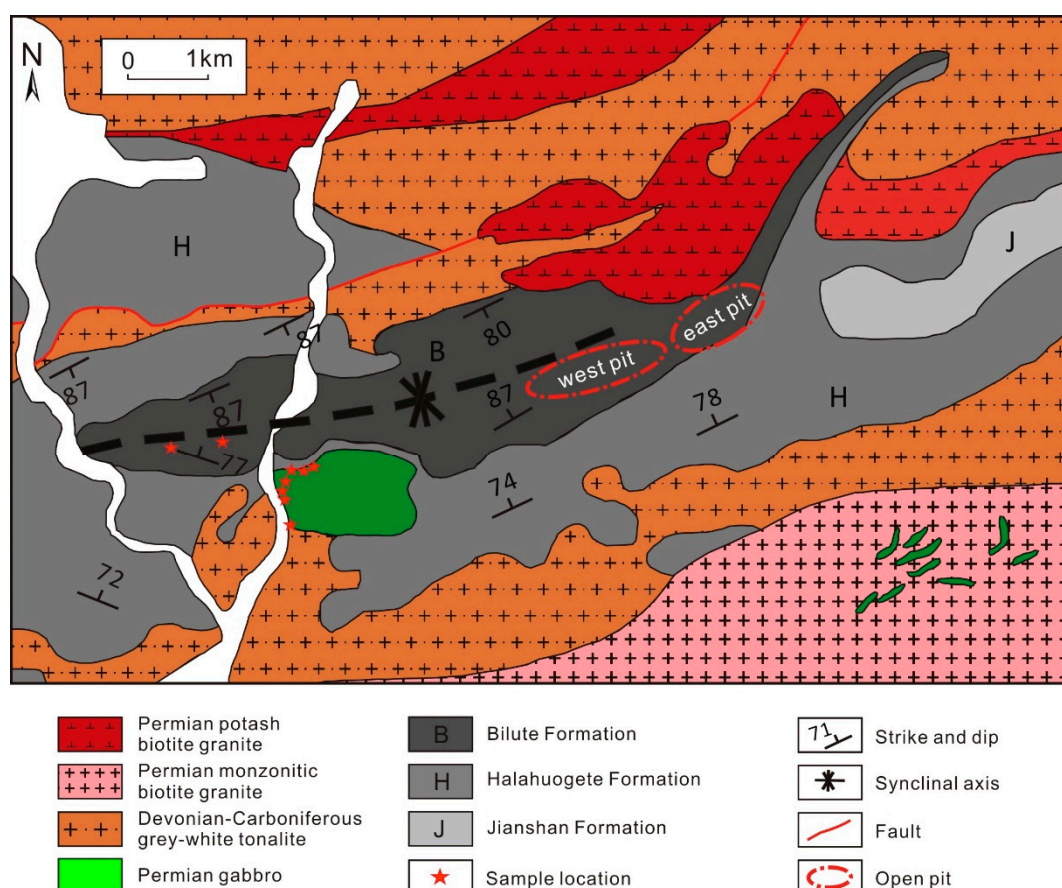


Figure 2. Geological map of the Haoyaoerhudong gold deposit showing the gabbro intrusion (modified after [14]).

In outcrops, the gabbro is characteristically dark-gray to black due to weathering (Figure 3B). Fresh surfaces of the rocks are gray or whitish gray with different contents of mafic minerals. No deformation has been observed in the oval intrusion or in the dikes, but some small felsic veins cut the gabbro

intrusions (Figure 3C). Thin section studies of the rocks show a medium-grained gabbroic assemblage, mainly including plagioclase, clinopyroxene, amphibole, and biotite (Figure 3D,E). Small amounts of pyrite and chalcopyrite were observed for the first time (Figure 3F) in this study. The mineral crystallization sequence of the Haoyaoerhudong gabbro appears to be clinopyroxene first, then plagioclase, and finally amphibole and biotite.

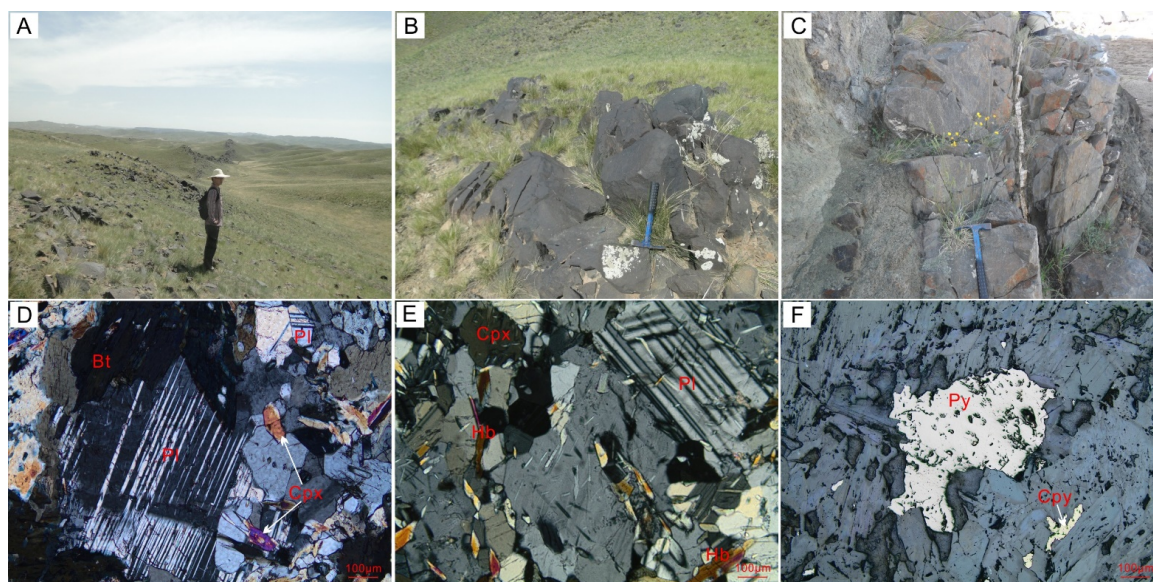


Figure 3. Representative field photographs and photomicrographs (cross-polarized light, D and E; single-polarized light, F) of the Haoyaoerhudong gabbro. (A) EW-trending gabbro dike; (B) Outcrop of the Haoyaoerhudong gabbro; (C) Thin felsic vein cut through the gabbro; (D,E) Mineral assemblage of the Haoyaoerhudong gabbro; (F) Metal minerals of the gabbro. Mineral abbreviations: Cpx, clinopyroxene; Bi, biotite; Hb, hornblende; Pl, plagioclase; Cpy, chalcopyrite; Py, pyrite.

3. Samples and Analytical Methods

In this study, a total of 10 representative samples were collected (8 from the Haoyaoerhudong gabbro and 2 from gabbro dikes 1 km west of the Haoyaoerhudong gabbro) for whole-rock major and trace elements, zircon dating, and bulk Sr–Nd isotopes. The samples were carefully examined to have the least alteration, cracks, and inclusions. The rock is massive, medium-fine grained, and equigranular. No cumulate textures were observed.

3.1. Whole-Rock Major and Trace Elements

Whole-rock major and trace elements were determined at the Langfang Institute of Geophysical and Geochemical Exploration, Hebei Province, China. Major elements were analyzed by X-ray fluorescence spectrometry. REEs and trace elements were tested by inductively coupled plasma-mass spectrometry. The general precision was better than 3% and 5% for major oxides and trace elements, respectively.

3.2. Zircon U–Pb Dating

Zircons were selected from sample RB25 using traditional techniques (density and magnetic separation) at the Langfang Institute of Regional Geology Survey, Hebei Province, China. All of the zircons were studied with micrographs and cathodoluminescence (CL) images to illustrate their microstructures. The zircon U–Th–Pb compositions were determined using a sensitive high-resolution ion microprobe at the Beijing SHRIMP Center. The analytical spot sizes were 30 μm , but each spot was rastered over 120 μm for three minutes to remove common Pb on the zircon surfaces. Five consecutive scans were performed for each zircon spot. The detailed analytical procedures are given in Jian et al. [29].

3.3. Sr–Nd Isotope

Sr–Nd isotopes were tested using an Isoprobe-T thermal ionization mass spectrometer (TIMS) at the Beijing Research Institute of Uranium Geology (BRIUG). Powder samples were mixed for isotope dilution and dissolved using HF + HNO₃ + HClO₄ in sealed Teflon capsules on a hot plate for 24 h. After separation of the Rb, Sr, and light REEs in a cation-exchange column, the Sm and Nd were further purified using a cation-exchange column, conditioned and eluted with dilute HCl. The TIMS was operated in static mode according to the standard procedures of GB/T17672-1999. Total chemical blanks were lower than 200 pg for strontium and lower than 50 pg for neodymium. The normalization standards are ¹⁴⁶Nd/¹⁴⁴Nd of 0.7219 and ⁸⁸Sr/⁸⁶Sr of 0.1194. Additional analytical details are given in Zhang et al. [30].

4. Results

4.1. SHRIMP U–Pb Age

The zircons from sample RB25 are euhedral to subhedral with length/width ratios of 1:1 to 2:1 (Figure 4). CL images show that some of the zircons have clear oscillatory zoning, indicating their magmatic origin [31]. The zircon SHRIMP U–Pb analytical data are presented in Table A1. The measured Th and U contents are 137–658 ppm and 153–477 ppm, respectively, and the Th/U ratios vary between 0.65 and 1.43. Sixteen analyses show clustered ²⁰⁶Pb/²³⁸U ages with a concordia age of 278.8 ± 0.81 Ma (MSWD = 0.117) (Figure 4), which is considered the crystallization age of the Haoyaoerhudong gabbro.

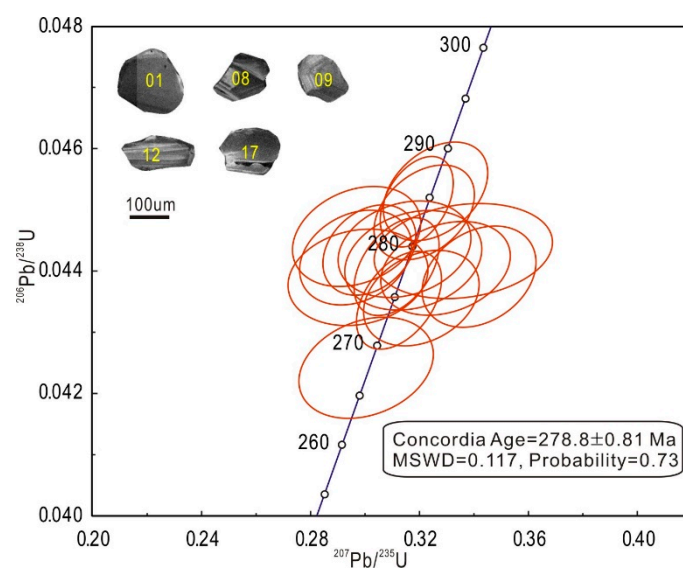


Figure 4. Representative cathodoluminescence (CL) images and U–Pb concordia diagram of zircons from sample RB25.

4.2. Major and Trace Element Data

As discussed above, the freshest available rock samples were selected for the chemical analysis. However, the sulfur minerals found in some thin sections suggest that the Haoyaoerhudong gabbro may suffer from hydrothermal alteration. Thus, it is important to evaluate the influence of postmagmatic alteration. In this study, all of the samples have LOI values much lower than 6 wt.% (ranging from 1.29 to 2.83 wt.%) and Ce/Ce* values concentrated in a narrow range from 0.9 to 1.0 (except samples RB04 and RB05, which have similar values of 0.87 and 1.03, respectively), indicating that these samples still have their primary chemical signatures without strong modification [32].

The major and trace element contents of the Haoyaoerhudong gabbro are reported in Table A2. The results show moderate variations in SiO_2 (44.76–51.0 wt.%) and relatively large variations of other oxides. The samples are characterized by relatively high contents of Al_2O_3 (average 13 wt.%, range 5.36–18.34 wt.%), CaO (average 11.12 wt.%, range 5.47–13.96 wt.%), and MgO (average 12.52 wt.%, range 4.98–24.78 wt.%) and low contents of Na_2O (average 1.25 wt.%, range 0.66–2.39 wt.%) and K_2O (average 0.43 wt.%, range 0.16–0.90 wt.%). Their Mg numbers ($100 \times \text{Mg}/[\text{Mg} + \text{Fe}^{2+}]$) range from 61 to 74 (excluding RB22, which has a very low value of 36). All of the points fall into the gabbro field in the Total Alkali vs Silica (TAS) diagram (Figure 5a). Most of the data plot in the calc-alkaline field on the Co–Th classification diagram [33], indicating calc-alkaline affinity (Figure 5b). On the MgO vs. major element oxides diagrams, CaO , K_2O , and Na_2O decrease and Fe_2O_3 (total iron) increases with increasing MgO (Figure 6), indicating fractionation processes of clinopyroxene and plagioclase with some Fe–Ti oxides.

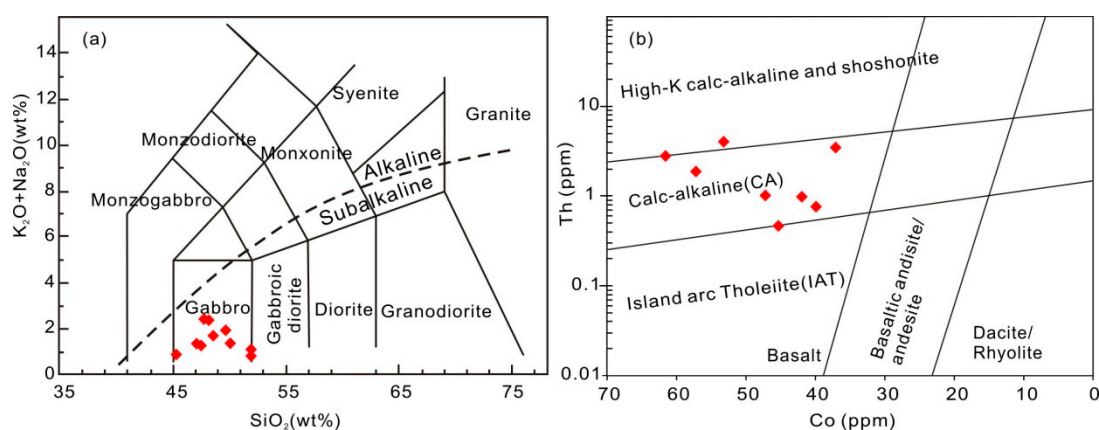


Figure 5. (a) TAS classification diagram and (b) Th–Co classification diagram (after [33]) for the Haoyaoerhudong gabbro.

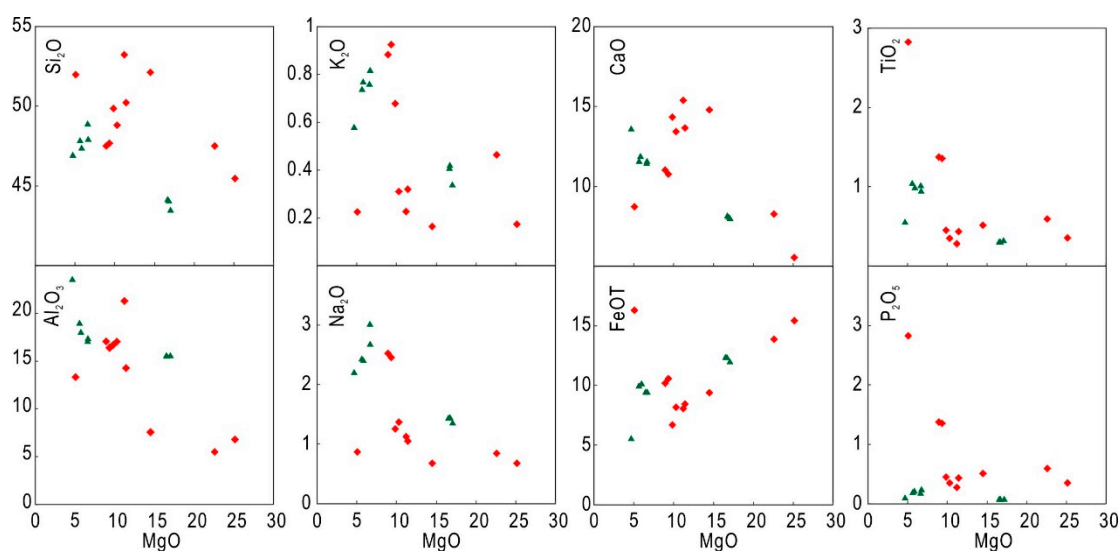


Figure 6. Harker diagrams for the Haoyaoerhudong gabbro. The data for the green triangles are from [34].

For compatible trace elements, the Cr contents vary in the range of 114–986 ppm (average 80 ppm), and Ni averages 161 ppm with a range of 30–530 ppm. For the high field strength elements, Nb averages 5.03 ppm with a large range of 0.51–16.79 ppm, and Zr averages 65 ppm with a range of 23.9–88.9 ppm. The large ion lithophile elements are relatively high. Ba ranges from 28.5 to 462.8 ppm (average of 251 ppm), and Sr ranges from 178 to 905 ppm (average of 560 ppm). On the primitive

mantle-normalized diagram (Figure 7a), all of the samples show similar features: enrichment of LILEs (Rb, Sr, and Ba) and depletion of HFSEs (Nb, Ta and P), indicating geochemical affinity to arc-type igneous rocks [35,36].

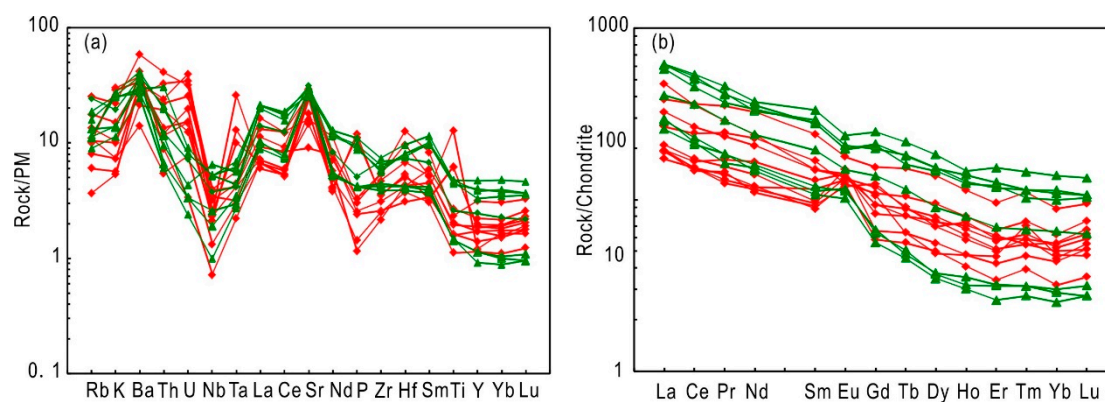


Figure 7. (a) PM-normalized incompatible element abundances and (b) chondrite-normalized REE patterns for the Haoyaoerhudong gabbro. The data for the green triangles are from [34]. The chondrite and PM values are from [37].

The REE distribution patterns show moderate fractionation between LREEs and HREEs with positive Eu anomalies (Figure 7b). The total REEs of the samples vary between 27.13 and 65.85 ppm with $(\text{La}/\text{Yb})_{\text{N}}$ ratios of 3.13 to 10.44. The Eu/Eu^* ratios have a range of 0.90–1.83 and an average of 1.25.

4.3. Sr–Nd Isotopic Data

Five samples (RB04, RB05, RB20, RB22, RB23) from the Haoyaoerhudong gabbro were tested for Sr–Nd isotopes (Table A3). The initial isotopic compositions were recalculated to 279 Ma based on the zircon U–Pb age from this study. The $(^{87}\text{Sr}/^{86}\text{Sr})_i$ ratios of the five tested samples vary between 0.7053 and 0.7078. The Nd isotopic compositions are relatively homogeneous, and the $^{143}\text{Nd}/^{144}\text{Nd}$ ratios have a small range of 0.5118–0.5123, corresponding to $\epsilon\text{Nd}(t)$ varying between -4.6 and -15.1 .

5. Discussion

5.1. Timing of a Hercynian Mafic Magmatic Event

Our new SHRIMP zircon data provide a precise age for the Haoyaoerhudong gabbro. The morphologies and internal structures, as well as the high Th/U values of the zircons from the Haoyaoerhudong gabbro, are suggestive of their magmatic origin. The 278.8 ± 0.81 Ma age (concordia age) indicates that the Haoyaoerhudong gabbro was emplaced in the Early Permian.

Previous studies have obtained age data for gabbros in the areas adjacent to the Haoyaoerhudong gold deposit. A 275.5 ± 1.8 Ma zircon U–Pb age (LA-ICP-MS) was obtained by Xiao [38] for the gabbro in the Nuoergong area (sample location N $39^{\circ}56'42''$, E $104^{\circ}47'20''$), which is thought to be a Permian continental magmatic arc. Zircon U–Pb dating (LA-ICP-MS) of two samples selected from the Taohaotuoquan gabbro yielded a consistent age of 276–275 Ma, suggesting emplacement in the Early Permian [39]. Zhao et al. [35] identified olive gabbro and amphibole gabbro in the Beiqigetao intrusion in the Wengeng area. They obtained a concordant SHRIMP U–Pb age of 269 ± 8 Ma for the olive gabbro (sample location N $41^{\circ}31'44''$, E $108^{\circ}05'24''$). All of these data demonstrate a wide range of Hercynian mafic magmatism in the studied area.

5.2. Magma Source and Petrogenesis

Magmatic rocks sourced from primary magma generally have high MgO, Mg#, Cr, and Ni contents (>15 wt.%, >65, >2000 ppm, and >500 ppm, respectively) [40]. The samples from the Haoyaoerhudong

gabbro have variable MgO contents (4.98–24.78, average of 13 wt.%), a wide Mg# range (35.7–74.4), Cr <1000 ppm, and Ni <500 ppm (Table A2). These data indicate that the Haoyaoerhudong gabbro underwent a differentiation process before its emplacement.

Several immobile elements, including Zr, Nb, and Yb, are widely used to study the attributes of the magma source, and element ratios (e.g., Nb/Yb) are considered to be indexes of mantle fertility of the rocks [41]. The Nb/Yb values of the studied gabbro cover a relatively wide range of 0.6–5.49 with an average of 2.95, which is similar to that of enriched mid-ocean ridge basalts (E-MORB, 3.5 [42]), indicating that the melt may be sourced from the mantle. The strong positive Sr and Eu anomalies of the Haoyaoerhudong gabbro are also similar to gabbros sourced from mantle-derived basaltic melt [43] (Figure 7a,b). Most of the samples plot in areas far from that of ocean island basalts (OIB) in the La/Ba vs. La/Nb diagram (Figure 8a), indicating lithospheric affinity rather than an asthenospheric mantle origin [44]. The Dy/Yb ratios of the tested samples are concentrated in a small range of 1.92–2.35, and the La/Yb ratios have a range of 5.11–14.36, indicating partial melting of spinel peridotite facies (Figure 8b) from a relatively shallow source [44,45].

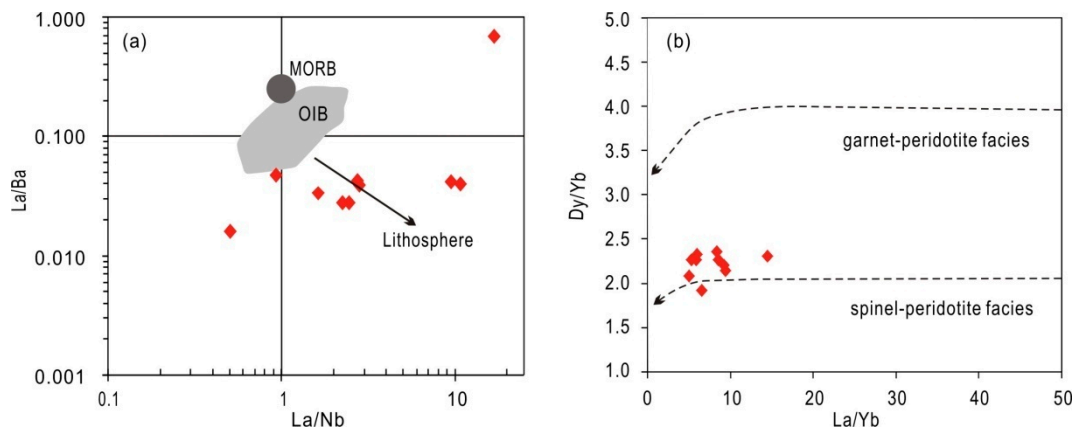


Figure 8. (a) La/Ba vs. La/Nb diagram and (b) Dy/Yb vs. La/Yb diagram showing the petrogenetic features of the Haoyaoerhudong gabbro. The fields in (a) are from [46]. The trends of the spinel-peridotite and garnet-peridotite facies in (b) are from [47].

It is widely accepted that crustal contamination should be considered in any intraplate setting [48]. Crustal contamination may lead to an increase in $(^{87}\text{Sr}/^{86}\text{Sr})_i$ and a decrease in $\epsilon\text{Nd}(t)$ in the magma [49] due to high $^{87}\text{Sr}/^{86}\text{Sr}$ and SiO_2 values and low $\epsilon\text{Nd}(t)$ and MgO values in crustal materials [50]. Thus, high $(^{87}\text{Sr}/^{86}\text{Sr})_i$ and low $\epsilon\text{Nd}(t)$ values may suggest the involvement of crustal materials. As illustrated by the $(^{87}\text{Sr}/^{86}\text{Sr})_i$ vs. $\epsilon\text{Nd}(t)$ plot, most of the points straddle the area from OIB to continental volcanics (Figure 9), indicating the influence of crustal materials in the formation of the Haoyaoerhudong gabbro.

Elemental ratios, such as Y/Nb, Nb/Zr, and La/Zr, are thought to be indexes of crustal contamination [51,52]. In the present case, the nearly constant or small ranges of these ratios (i.e., 1.77–5.52 for Y/Nb, except for one value of 15.18; 0.02–0.12 for Nb/Zr; and 0.10–0.22 for La/Zr) indicate that crustal contamination may have played a crucial role in the generation of the Haoyaoerhudong gabbro. It has been suggested that Lu–Yb ratios will not change dramatically during partial melting or fractional crystallization [53]. Mantle-derived magma and the continental crust have relatively low (0.14–0.15) and high (0.16–0.18) Lu/Yb ratios, respectively [42,54]. The Lu/Yb ratios in this study (0.14–0.19, average of 0.17) indicate crustal addition during the formation of the Haoyaoerhudong gabbro. The high Th/Ta ratios (1.83–19.22, average of 8.23) and low Nb* ($\text{Nb}^* = \text{Nb}_{\text{PM}} / \sqrt{(\text{Th}_{\text{PM}} \times \text{La}_{\text{PM}})})$ values of the gabbro (0.09–0.84, average of 0.36) also suggest the involvement of crustal materials [55].

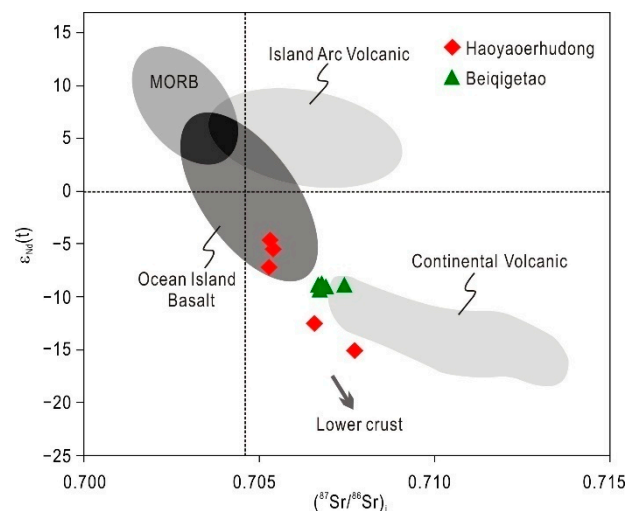


Figure 9. $\epsilon_{\text{Nd}}(t)$ vs. $(^{87}\text{Sr}/^{86}\text{Sr})_i$ diagram for the Haoyaoerhudong gabbro. The contents of MORB, OIB, island arc volcanics and continental volcanics are from [15,56,57]. The trend to the lower crust is from [58]. The data for the green triangles are from [34].

The decoupling between Nb and Ta and between Zr and Hf are widely used as indexes for subduction processes [59]. The scattered Nb/Ta ratios (5.67–26.12) and Zr/Hf ratios (15.45–30.21) of the studied samples differ from that of the primitive mantle (Nb/Ta of 17.8 and Zr/Hf of 37) [37] and crust (Nb/Ta of 11 and Zr/Hf of 33) [60], indicating that they might be related to subduction processes. Generally, subducted slab-released fluids lead to high Rb, Sr, Ba, U, and Pb contents, whereas subducted oceanic sediment-derived melts lead to high concentrations of LREEs and Th in the magma. Experiments show that the Ce/Pb values of slab-dehydrated fluids are usually lower than 0.1 [61], and Ce/Pb ratios less than 20 may indicate the involvement of subduction-dehydrated fluids [62]. Therefore, the Ce/Pb ratios of the studied samples (1.35–7.38, average of 3.84) which are lower than that of mantle-sourced magmas (e.g., oceanic basalts have Ce/Pb ratios of approximately 25) might be caused by the addition of Pb via subduction fluids [61]. Mantle metasomatism of the Haoyaoerhudong gabbro was further indicated by the Ba/Th versus La/Sm plot [63] and the Th/Yb versus Sr/Nd plot [64]. As shown in Figure 10a,b, the points of the Haoyaoerhudong samples are consistent with the slab dehydration trend and distinctly different from the sediment melting trend, indicating that the mantle was modified by fluids from slab dehydration. In addition, the presence of hornblende and biotite in most thin sections showed water-rich features of the parent magma, suggesting the effect of slab hydration during magma genesis.

Both the major and trace element contents of the Haoyaoerhudong gabbro vary over large ranges, indicating fractional crystallization processes. Ni and Cr are positively related to MgO in the Haoyaoerhudong gabbro, indicating fractional crystallization of clinopyroxene. The negative correlation of MgO and Al_2O_3 as well as the positive Eu anomaly of the Haoyaoerhudong gabbro demonstrates plagioclase fractional crystallization. In summary, we suggest that the Haoyaoerhudong gabbro originated from partial melting of a spinel peridotite facies of the mantle, which was metasomatized by fluids that dehydrated from a subducted slab. Fractionation crystallization is the most likely petrogenesis mechanism for the Haoyaoerhudong gabbro.

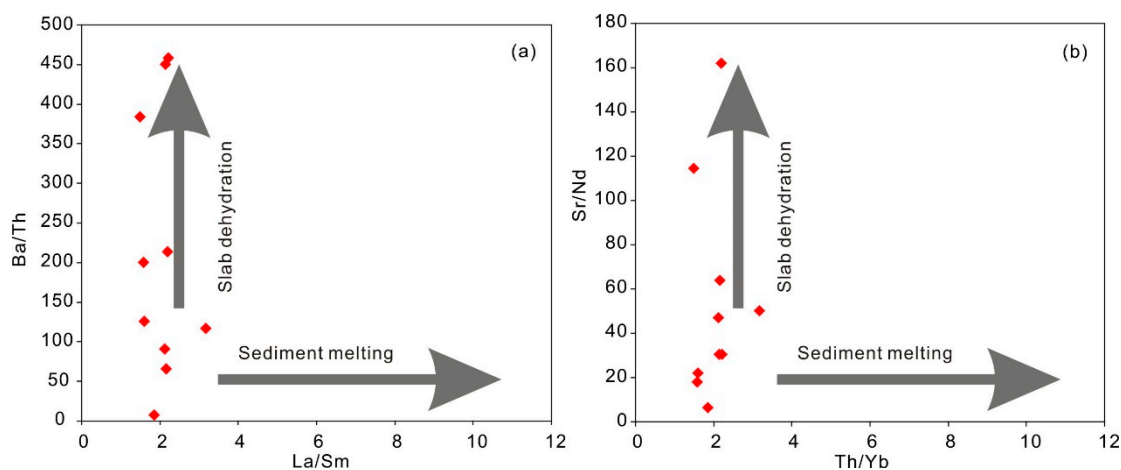


Figure 10. (a) Plot of Ba/Th vs. La/Sm for the Haoyaoerhudong gabbro (after [63]). (b) Plot of Th/Yb vs. Sr/Nd for the Haoyaoerhudong gabbro (after [64]).

5.3. Implications for the Tectonic Setting

Generally, Th and Nb are geochemically similar. However, Th becomes mobile in subduction magmatic processes due to the addition of hydrous fluids from the subducted slab, whereas Nb is stable during this process [65]. Thus, Th and Nb are widely used to identify mafic rocks of different tectonic units [55]. To understand the tectonic setting of the Haoyaoerhudong gabbro, we applied the Th_N-Nb_N discrimination plot [66]. Three samples spread along the MORB-OIB array, two points plot in the forearc and intra-arc field, and five samples fall into the continental margin volcanic arc field (Figure 11). This plot also indicates that the Haoyaoerhudong magma was affected by fluids that dehydrated from the subducting slab.

Jenner et al. reported that arc gabbros and non-arc gabbros have different Nb/Th values (<7.5 and >8.5 , respectively) [67]. Most of the Nb/Th values of the Haoyaoerhudong gabbro are <7.5 (eight of the 10 tested samples range from 0.65 to 4.18, and two samples are slightly higher than 7.5), which indicates their arc affinities. In the Hf–Nb–Th diagram (Figure 12), two samples fall into the E-MORB field, and the other eight points fall into the CAB (calc-alkaline basalts) field, indicating that they likely formed in a continental arc environment. Other geochemical characteristics of the Haoyaoerhudong gabbro that are consistent with rocks from a continental arc include the enrichment of LILEs and LREEs, depletion of HSFES, high La/Nb ratios (1.2–5.0 with an average of 3.5, which is higher than that of N-MORB, which has La/Nb ratios lower than 1.4), and negative $\epsilon Nd(t)$ values of -4.6 to -15.1 [41].

The time that the Paleo-Asian Ocean (PAO) closed in the Xingmeng Orogenic Belt (XOB) has long been a controversial topic. A diachronous closure of the PAO, from west (Tarim) to east (Changchun), was suggested by Xiao et al. [26] and Wilde [68]. Luo et al. obtained a U–Pb zircon age of 277 ± 3 Ma for the Wuliangsitai intrusion, which was identified as an A_2 -type (postcollisional) granitoid, indicating a post-orogenic extensional setting [69]. Recently, Liu et al. noticed a sharp change of the $\epsilon Hf(t)$ (in zircon) and $\epsilon Nd(t)$ (whole-rock) values of the 280–265 Ma gabbros from the Alxa Terrane and inferred a tectonic change from subduction to post-collision [70]. The Haoyaoerhudong gabbro has similar REE and trace element distributions and Sr–Nd isotopic features (Figures 7 and 9) as the Beiqigetao gabbro [34], which was interpreted as a Permian postcollisional intrusion. In addition, no obvious deformation has been observed in the Haoyaoerhudong gabbro. The gabbroic dikes are steep and sharp. All of this information suggests that the Haoyaoerhudong gabbro is the product of post-collisional mafic magmatism. Thus, it can be inferred that the PAO closed before 278.8 ± 0.81 Ma in the western section of the XOB.

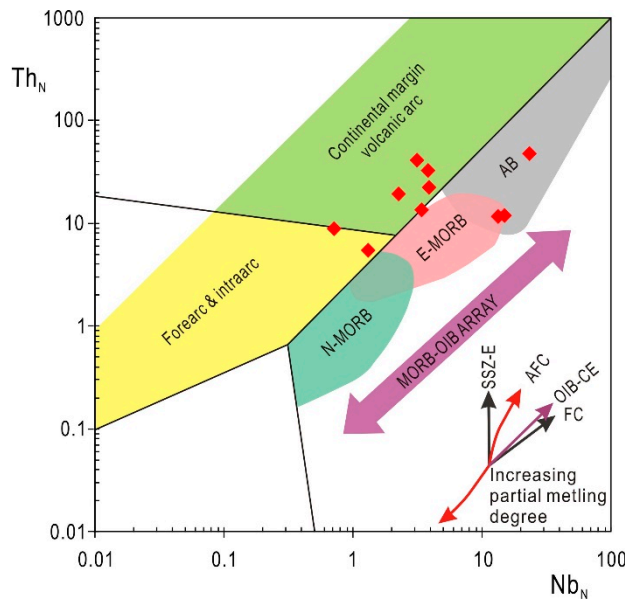


Figure 11. Th_N vs. Nb_N plot for the Haoyaoerhudong gabbro (after [66]). The N-MORB composition is from [42].

The post-collisional setting is also supported by the gold mineralization features. In the Haoyaoerhudong gold deposit, most of the thin gold-bearing sulfide veins (films) are located on E-W-trending open bedding planes and schistosity planes, which suggests that the gold mineralization, along with the late stage magmatic activities, formed in a post-collisional extensional setting.

6. Conclusions

1. The SHRIMP U–Pb zircon age shows that the Haoyaoerhudong gabbro in the Haoyaoerhudong gold deposits intruded into Proterozoic strata at 279 ± 2 Ma, indicating a Permian mafic magmatic event in the western section of the northern margin of the NCC.

2. The Haoyaoerhudong gabbro is subalkaline with calc-alkaline affinity, and its source magma was probably the result of the partial melting of the spinel peridotite zone of the lithospheric mantle, which was modified by subducting fluids.

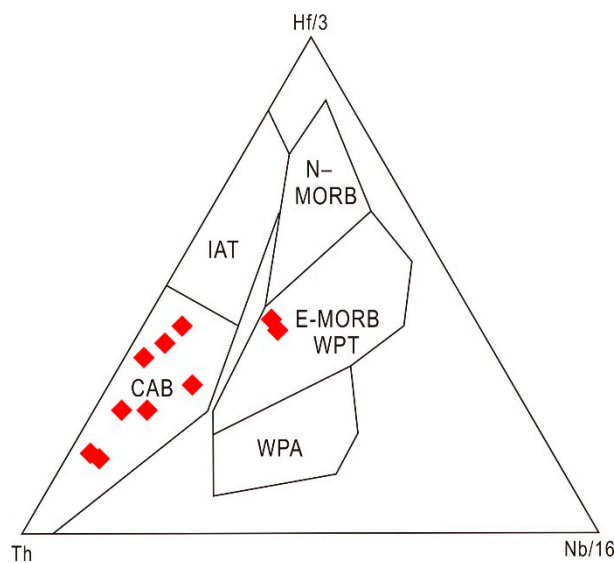


Figure 12. Th–Hf–Nb triangular discrimination diagram (after [71]) for the Haoyaoerhudong gabbro.

3. Both the Haoyaoerhudong gold deposit and the Haoyaoerhudong gabbro were generated in a post-collisional geodynamic setting, most likely induced by subduction and rollback of the paleo-oceanic plate beneath the NCC.

Author Contributions: Conceptualization, J.W.; Data curation, X.W.; Formal analysis, Z.L.; Investigation, J.W. and X.W.; Methodology, J.L.; Supervision, J.L.; Writing—original draft, J.W.; Writing—review and editing, Z.L., D.Z. and Y.W.

Funding: This study was funded by the National Natural Science Foundation of China (No. 41730426, 41272106, 41030423).

Acknowledgments: The authors are grateful to manager Xiangdong Jiang and Qiang Li of the Inner Mongolia Pacific Mining Co. Ltd. for permission to access the mining project. Engineer Hailong Gao and Zhihui Dou are thanked for their help during the fieldwork.

Conflicts of Interest: The authors declare no conflict of interest.

Appendix A

Table A1. SHRIMP zircon U–Pb isotope data for the Haoyaoerhudong gabbro.

Spot	U	Th	U/Th	Pb*	Pbc	$^{206}\text{Pb}/^{238}\text{U}$ $\pm\%$	$^{207}\text{Pb}/^{235}\text{U}$ $\pm\%$	$^{207}\text{Pb}/^{206}\text{Pb}$ $\pm\%$	$^{206}\text{Pb}/^{238}\text{U}$ age (Ma)	$\pm\%$			
RB25-1	188	203	1.11	7.03	–	0.04353	1.3	0.313	3.3	0.0585	2.6	274.7	3.4
RB25-2	257	293	1.17	9.84	0.61	0.04421	1.2	0.297	4.7	0.0538	3.8	278.9	3.2
RB25-3	214	200	0.97	8.04	–	0.04390	1.2	0.342	4.0	0.0548	3.7	277.0	3.3
RB25-4	405	521	1.33	15.5	0.49	0.04438	1.1	0.315	5.2	0.0574	2.8	279.9	3
RB25-5	306	331	1.12	11.6	0.16	0.04403	1.2	0.330	4.6	0.0571	2.3	277.7	3.2
RB25-6	186	212	1.18	6.80	0.29	0.04242	1.3	0.300	5.4	0.0532	3.0	267.8	3.4
RB25-9	378	471	1.29	14.6	–	0.04514	1.1	0.3193	2.6	0.0553	2.0	284.6	3
RB25-10	285	368	1.33	10.9	0.54	0.04432	1.2	0.337	6.4	0.0631	3.8	279.6	3.2
RB25-11	328	349	1.10	12.8	0.19	0.04532	1.1	0.326	3.9	0.0556	2.1	285.8	3.1
RB25-13	259	275	1.10	9.69	0.15	0.04355	1.2	0.321	4.4	0.0541	2.6	274.8	3.2
RB25-14	343	350	1.05	13.1	0.56	0.04416	1.1	0.318	5.3	0.0597	2.0	278.5	3.1
RB25-15	324	388	1.24	12.5	0.05	0.04495	1.1	0.322	3.9	0.0572	2.6	283.4	3.1
RB25-17	380	436	1.18	14.5	0.29	0.04432	1.1	0.302	3.8	0.0542	2.0	279.6	3
RB25-18	191	215	1.16	7.23	–	0.04409	1.2	0.312	3.3	0.0506	3.0	278.1	3.4
RB25-19	207	239	1.20	7.95	0.59	0.04456	1.2	0.298	5.1	0.0581	2.6	281.0	3.4
RB25-20	272	290	1.10	10.3	0.32	0.04391	1.2	0.298	5.8	0.0512	2.5	277.0	3.2

Errors are 1σ . Pbc and Pb* are common Pb and radiogenic Pb, respectively. ^{204}Pb correction used for the zircon ages.

Table A2. Major (wt.%) and trace (ppm) element compositions for the Haoyaoerhudong gabbro.

Sample	RB4	RB5	RB7	RB8	RB9	RB10	RB20	RB22	RB23	RB25
SiO ₂	46.44	46.30	44.76	48.80	50.64	46.19	51.00	47.33	45.93	48.51
Al ₂ O ₃	15.95	16.61	6.70	13.87	7.36	5.36	13.07	16.50	18.34	16.24
TiO ₂	1.32	1.34	0.35	0.42	0.50	0.58	2.77	0.34	0.24	0.44
Fe ₂ O ₃	1.97	1.74	1.53	0.44	0.71	1.49	2.43	1.40	1.26	0.66
FeO	8.50	8.36	13.79	7.78	8.46	12.15	13.80	6.65	5.80	5.93
CaO	10.49	10.75	5.47	13.27	14.36	8.03	8.56	13.02	13.28	13.96
MgO	9.10	8.71	24.78	11.11	14.11	21.99	4.98	9.97	10.91	9.56
K ₂ O	0.90	0.86	0.17	0.31	0.16	0.45	0.22	0.30	0.22	0.66
Na ₂ O	2.39	2.46	0.67	1.02	0.66	0.82	0.85	1.33	1.09	1.22
MnO	0.15	0.14	0.21	0.11	0.17	0.17	0.22	0.14	0.11	0.10
P ₂ O ₅	0.26	0.24	0.05	0.07	0.07	0.06	0.24	0.03	0.03	0.07
LOI	2.31	2.28	1.29	2.55	2.59	2.44	1.72	2.83	2.63	2.46
Total	99.78	99.79	99.77	99.75	99.79	99.71	99.87	99.83	99.84	99.82
Be	0.73	0.60	0.20	0.37	0.41	0.23	0.82	0.20	0.22	0.38
Co	47.10	41.85	115.80	61.50	57.10	92.90	53.10	39.70	45.20	37.00
Ni	86.00	70.85	530.10	233.80	150.00	365.70	71.00	32.20	37.70	29.70
Cr	227.30	181.80	868.80	985.60	526.60	117.00	114.20	196.10	289.70	294.40
V	279.50	264.40	106.90	233.60	244.30	172.70	487.60	212.60	140.60	159.00
Sc	38.34	36.24	21.05	46.40	66.63	33.84	37.90	37.71	30.54	34.67

Table A2. Cont.

Sample	RB4	RB5	RB7	RB8	RB9	RB10	RB20	RB22	RB23	RB25
Li	10.83	9.44	5.95	3.98	4.10	4.96	22.73	5.22	6.91	9.56
Cs	0.50	0.42	0.19	0.99	0.26	0.45	0.11	0.56	0.40	1.10
Ga	21.33	19.45	7.41	14.21	9.91	6.73	25.27	15.83	16.01	12.11
In	0.07	0.07	0.03	0.04	0.06	0.04	0.11	0.04	0.03	0.03
Tl	0.11	0.09	0.05	0.05	0.17	0.09	0.10	0.06	0.04	0.13
Cu	41.20	37.49	51.10	149.80	88.00	81.50	20.00	14.00	15.70	37.00
Pb	6.10	6.00	3.10	6.80	3.80	4.10	12.00	5.80	5.20	16.10
Zn	106.70	96.11	134.80	69.80	75.80	112.60	183.40	60.10	47.40	59.40
Rb	13.30	10.90	3.80	8.50	2.30	11.20	6.90	6.60	5.10	16.00
Sr	825.50	798.90	306.60	615.60	334.70	190.60	177.90	887.00	904.50	554.80
Zr	88.90	88.80	28.70	59.40	60.10	34.40	190.10	23.90	27.80	52.00
Nb	10.71	9.51	1.63	2.74	2.81	2.45	16.79	0.51	0.94	2.25
Ta	0.41	0.53	0.17	0.17	0.23	0.13	1.06	0.09	0.12	0.18
Ba	462.80	436.40	148.20	180.80	235.40	227.80	28.50	288.10	98.20	404.50
Hf	3.64	3.58	0.95	2.95	3.89	1.30	6.53	1.32	1.14	2.07
W	0.17	0.19	0.14	0.14	0.43	0.19	0.53	0.17	0.25	0.22
Bi	0.05	0.04	0.03	0.22	0.09	0.04	0.21	0.08	0.06	0.08
Th	1.01	0.97	1.64	2.77	1.87	1.14	4.02	0.75	0.46	3.46
U	0.41	0.31	0.26	0.72	0.53	0.32	0.82	0.07	0.16	0.66
La	18.54	18.10	4.92	7.67	9.08	6.31	19.48	4.59	4.58	11.21
Ce	45.00	43.41	10.57	16.21	22.05	14.89	44.39	10.20	9.37	21.70
Pr	6.38	6.18	1.48	2.22	3.35	2.33	6.24	1.62	1.33	2.73
Nd	27.14	26.36	6.53	9.64	15.19	10.65	27.52	7.75	5.59	11.11
Sm	5.41	5.46	1.50	2.29	3.67	2.58	6.76	1.98	1.35	2.28
Eu	1.77	1.77	0.47	0.82	1.03	0.72	2.26	0.82	0.71	0.79
Gd	4.53	4.43	1.35	1.92	3.18	2.23	6.47	1.70	1.20	1.92
Tb	0.73	0.74	0.24	0.33	0.57	0.39	1.24	0.30	0.21	0.30
Dy	4.18	4.27	1.42	2.01	3.49	2.40	7.93	1.92	1.27	1.77
Ho	0.80	0.80	0.27	0.38	0.64	0.45	1.47	0.35	0.23	0.33
Er	2.02	1.98	0.70	0.95	1.58	1.10	3.77	0.85	0.56	0.83
Tm	0.34	0.35	0.12	0.16	0.28	0.19	0.68	0.14	0.10	0.15
Yb	1.95	1.94	0.74	0.89	1.50	1.06	3.81	0.85	0.54	0.77
Lu	0.37	0.36	0.13	0.15	0.24	0.19	0.52	0.13	0.09	0.14
Y	18.93	18.35	6.31	8.55	14.21	10.06	34.39	7.74	5.19	7.77
ΣREE	29.58	29.47	30.84	45.64	65.85	45.49	28.94	33.20	27.13	56.03
LREE	22.16	22.28	25.87	38.85	54.37	37.48	23.15	26.96	22.93	49.82
HREE	7.42	7.19	4.97	6.79	11.48	8.01	5.79	6.24	4.20	6.21
LREE/HREE	2.99	3.10	5.21	5.72	4.74	4.68	4.00	4.32	5.46	8.02
LaN/YbN	3.43	3.13	4.77	6.18	4.34	4.27	3.97	3.87	6.08	10.44
δEu	1.11	1.24	1.83	1.16	0.90	0.90	1.19	1.33	1.67	1.12
δCe	0.87	1.03	0.95	0.95	0.98	0.95	0.96	0.92	0.92	0.93

Table A3. Rb–Sr and Sm–Nd isotopes for the Haoyaoerhudong gabbro.

Sample	Age (Ma)	SiO ₂ (wt.%)	Rb (μg/g)	Sr (μg/g)	⁸⁷ Rb/ ⁸⁶ Sr	⁸⁷ Sr/ ⁸⁶ Sr	Error	(⁸⁷ Sr/ ⁸⁶ Sr) _i	Sm (μg/g)	Nd (μg/g)	¹⁴⁷ Sm/ ¹⁴⁴ Nd	¹⁴³ Nd/ ¹⁴⁴ Nd	Error	(¹⁴³ Nd/ ¹⁴⁴ Nd) _i	εNd(0)	εNd(t)	f _{Sm/Nd}	T _{DM}
RB04	279	46.44	6.3	525.5	0.033844	0.70789	0.00002	0.70776	1.41	5.14	0.173697	0.51182	0.00001	0.511503	−16	−15.1	−0.12	5017
RB05	279	46.3	6.9	598.9	0.032524	0.70673	0.00002	0.70666	1.46	5.36	0.172474	0.51195	0.00001	0.511635	−13.4	−12.6	−0.12	4401
RB20	279	51	6.9	377.9	0.051544	0.70551	0.00003	0.70531	1.76	5.52	0.201888	0.51228	0.00004	0.511911	−7	−7.2	−0.03	10,968
RB22	279	47.33	6.6	587	0.031741	0.70554	0.00002	0.70541	1.98	7.75	0.161771	0.51229	0.00002	0.511995	−6.8	−5.5	−0.18	2519
RB23	279	45.93	5.1	504.5	0.028538	0.70544	0.00002	0.70533	1.35	5.59	0.152918	0.51232	0.00002	0.512041	−6.2	−4.6	−0.22	2080

References

1. Liu, D.Y.; Nutman, A.P.W.; Compston, W.; Wu, J.S.; Shen, Q.H. Remnants of ≥ 3800 Ma crust in the Chinese part of the Sino-Korean Craton. *Geology* **1992**, *20*, 339–342. [[CrossRef](#)]
2. Zhai, M.G.; Santosh, M. The early Precambrian odyssey of the North China Craton: A synoptic overview. *Gondwana Res.* **2011**, *20*, 6–25. [[CrossRef](#)]
3. Zhai, M.G.; Santosh, M. Metallogeny of the North China Craton: Link with secular changes in the evolving Earth. *Gondwana Res.* **2013**, *24*, 275–297. [[CrossRef](#)]
4. Zhao, G.C.; Sun, M.; Wilde, S.A.; Li, S.Z. Late Archean to Paleoproterozoic evolution of the North China Craton: Key issues revisited. *Precambrian Res.* **2005**, *136*, 177–202. [[CrossRef](#)]
5. Li, J.Y.; Zhang, J.; Yang, T.N.; Li, Y.P.; Sun, G.H.; Zhu, Z.X.; Wang, L.J. Crustal tectonic division and evolution of the southern part of the North Asian Orogenic Region and its adjacent areas. *J. Jilin Univ.* **2009**, *39*, 584–605.
6. Zhang, S.H.; Zhao, Y.; Liu, J.M.; Hu, J.M.; Song, B.; Liu, J.; Wu, H. Geochronology, geochemistry and tectonic setting of the Late Paleozoic–Early Mesozoic magmatism in the northern margin of the North China Block: A preliminary review. *Acta Petrol. Mineral.* **2010**, *29*, 824–842. (In Chinese with English abstract)
7. Zhang, J.J.; Wang, T.; Zhang, Z.C.; Tong, Y.; Zhang, L.; Shi, X.J.; Zeng, T. Magma mixing origin of Yamatu granite in Nuoergong–Langshan area, western part of the Northern Margin of North China Craton: Petrological and geochemical evidences. *Geol. Rev.* **2012**, *58*, 53–66. (In Chinese with English abstract)
8. Shi, Y.R.; Liu, C.; Deng, J.F.; Jian, P. Geochronological frame of granitoids from Central Inner Mongolia and its tectonomagmatic evolution. *Acta Petrol. Sin.* **2014**, *30*, 3155–3171.
9. Wang, J.P.; Liu, J.J.; Peng, R.M.; Liu, Z.J.; Zhao, B.S.; Li, Z.; Wang, Y.F.; Liu, C.H. Gold mineralization in Proterozoic black shales: Example from the Haoyaoerhudong gold deposit, northern margin of the North China Craton. *Ore Geol. Rev.* **2014**, *63*, 150–159. [[CrossRef](#)]
10. Wang, Y.F.; Wang, J.P.; Li, Y.M.; Jiang, X.D.; Wang, B.; Jiang, S.M. Organic geochemical characteristics and metallogenetic significance of the ore-hosting strata of the Haoyaoerhudong gold deposit, Inner Mongolia. *Acta Miner. Sin.* **2011**, *31*, 405–407. (In Chinese)
11. Wang, Y.F.; Wang, J.P.; Wang, H.; Sun, H.; Jiang, X.D.; Wang, B.; Jiang, S.M. Geochemical characteristics of pluton in the Haoyaoerhudong gold deposit of Inner Mongolia and its ore-forming significance. *Geoscience* **2013**, *27*, 56–66. (In Chinese with English abstract).
12. Xiao, W.; Nie, F.J.; Liu, Y.F.; Liu, Y. Isotope geochronology study of the granitoid intrusions in the Changshanhao gold deposit and its geological implications. *Acta Petrol. Sin.* **2012**, *28*, 535–543.
13. Cao, Y.; Nie, F.J.; Xiao, W.; Liu, Y.F.; Zhang, W.B.; Wang, F.X. Metallogenic age of the Changshanhao gold deposit in Inner Mongolia, China. *Acta Petrol. Sin.* **2014**, *30*, 2092–2100. [[CrossRef](#)]
14. Liu, Y.F.; Nie, F.J.; Jiang, S.H.; Bagas, L.; Xiao, W.; Cao, Y. Geology, geochronology and sulphur isotope geochemistry of the black schist-hosted Haoyaoerhudong gold deposit of Inner Mongolia, China: Implications for ore genesis. *Ore Geol. Rev.* **2016**, *73*, 253–269. [[CrossRef](#)]
15. Hart, S.R.; Gerlach, D.C.; White, W.M. A possible new Sr–Nd–Pb mantle array and consequences for mantle mixing. *Geochim. Cosmochim. Acta* **1986**, *50*, 1551–1557. [[CrossRef](#)]
16. Robinson, P.T.; Zhou, M.F. The origin and tectonic setting of ophiolites in China. *J. Asian Earth Sci.* **2008**, *32*, 301–307. [[CrossRef](#)]
17. Halama, R.; Wenzel, T.; Upton, B.G.J.; Siebel, W.; Markl, G. A geochemical and Sr–Nd–O isotopic study of the Proterozoic Eriksfjord Basalts, Gardar Province, South Greenland: Reconstruction of an OIB signature in crustally contaminated rift-related basalts. *Miner. Mag.* **2003**, *67*, 831–853. [[CrossRef](#)]
18. Wang, J.; Li, S.Q.; Wang, B.L.; Li, J.J. *The Langshan-Baiyunebo Rift System*; Peking University Press: Beijing, China, 1992; pp. 1–129.
19. Gong, W.B.; Hu, J.M.; Li, Z.H.; Dong, X.P.; Liu, Y.; Liu, S.C. Detrital zircon U–Pb dating of Zhaertai Group in the north margin rift zone of North China Craton and its implications. *Acta Petrol. Sin.* **2016**, *32*, 2151–2165.
20. Meng, Q.R.; Wei, H.H.; Qu, Y.Q.; Ma, S.X. Stratigraphic and sedimentary records of the rift to drift evolution of the northern North China craton at the Paleo- to Mesoproterozoic transition. *Gondwana Res.* **2011**, *20*, 205–218. [[CrossRef](#)]
21. Liu, C.H.; Liu, F.L. The Mesoproterozoic rifting in the North China Craton: A case study for magmatism and sedimentation of the Zhaertai-Bayan Obo-Huade rift zone. *Acta Petrol. Sin.* **2015**, *31*, 3107–3128.

22. Bai, G.; Yuan, Z.X.; Wu, C.Y.; Zhang, Z.Q.; Zheng, L.X. *Demonstration on the Geological Features and Genesis of the Bayan Obo ore Deposit*; Geological Publishing House: Beijing, China, 1996; pp. 1–92.
23. Yang, X.M.; Le, B.M.J. Chemical compositions of carbonate minerals from Bayan Obo, Inner Mongolia, China: Implications for petrogenesis. *Lithos* **2004**, *72*, 97–116. [[CrossRef](#)]
24. Smith, M.P.; Campbell, L.S.; Kynicky, J. A review of the genesis of the world class Bayan Obo Fe-REE-Nb deposits, Inner Mongolia, China: Multistage processes and outstanding questions. *Ore Geol. Rev.* **2015**, *64*, 459–476. [[CrossRef](#)]
25. Peng, R.M.; Zhai, Y.S. The confirmation of the metamorphic double-peaking volcanic rocks in langshan Group of the Dongshengmiao ore district, Inner Mongolia, and its significance. *Earth Sci. J. China Univ. Geosci.* **1997**, *22*, 589.
26. Xiao, W.J.; Windley, B.F.; Hao, J.; Zhai, M.G. Accretion leading to collision and the Permian Solonker suture, Inner Mongolia, China: Termination of the central Asian orogenic belt. *Tectonics* **2003**, *22*, 1069. [[CrossRef](#)]
27. Xiao, W.J.; Kroner, A.; Windley, B. Geodynamic evolution of Central Asia in the Paleozoic and Mesozoic. *Int. J. Earth Sci.* **2009**, *98*, 1185–1188. [[CrossRef](#)]
28. Nie, F.J.; Jiang, S.H.; Huo, W.R.; Liu, Y.F.; Xiao, W. Geological features and genesis of gold deposits hosted by low-grade metamorphic rocks in central-western Inner Mongolia. *Miner. Depos.* **2010**, *29*, 58–70.
29. Jian, P.; Kröner, A.; Zhou, G.Z. SHRIMP zircon U–Pb ages and REE partition for high-grade metamorphic rocks in the north Dabie complex: Insight into crustal evolution with respect to Triassic UHP metamorphism in east-central China. *Chem. Geol.* **2012**, *328*, 49–69. [[CrossRef](#)]
30. Zhang, L.H.; Guo, Z.F.; Zhang, M.L.; Cheng, Z.H.; Sun, Y.T. Post-collisional potassic magmatism in the eastern Lhasa terrane, South Tibet: Products of partial melting of melanges in a continental subduction channel. *Gondwana Res.* **2017**, *41*, 9–28. [[CrossRef](#)]
31. Hoskin, P.W.O.; Schaltegger, U. The composition of zircon and igneous and metamorphic petrogenesis. *Rev. Miner. Geochem.* **2003**, *53*, 27–62. [[CrossRef](#)]
32. Polat, A.; Hofmann, A.W. Alteration and geochemical patterns in the 3.7–3.8 Ga Isua greenstone belt, West Greenland. *Precambrian Res.* **2003**, *126*, 197–218. [[CrossRef](#)]
33. Hastie, A.R.; Kerr, A.C.; Pearce, J.A.; Mitchell, S.F. Classification of altered volcanic island arc rocks using immobile trace elements: Development of Th–Co discrimination diagrams. *J. Petrol.* **2007**, *48*, 2341–2357. [[CrossRef](#)]
34. Zhao, L.; Wu, T.R.; Luo, H.L. SHRIMP U–Pb dating, geochemistry and tectonic implications of the Beiqigetaogabbros in UradZhongqi area, Inner Mongolia. *Acta Petrol. Sin.* **2011**, *27*, 3071–3082. (In Chinese with English abstract)
35. Rudnick, R.L. Making continental crust. *Nature* **1995**, *378*, 571–578. [[CrossRef](#)]
36. Taylor, S.R.; McLennan, S.M. The geochemical evolution of the continental crust. *Rev. Geophys.* **1995**, *33*, 241–265. [[CrossRef](#)]
37. McDonough, W.F.; Sun, S.S. The composition of the earth. *Chem. Geol.* **1995**, *120*, 223–253. [[CrossRef](#)]
38. Xiao, J.; Sun, P.; Xu, L. LA-ICP-MS zircon U–Pb age, geochemistry and genesis of the early Permian gabbros in the Nuoergong area, northern Alex. *West. Resour.* **2011**, *4*, 55–60. (In Chinese)
39. Zhang, L.; Shi, X.J.; Zhang, J.J.; Yang, Q.D.; Tong, Y.; Wang, T. LA-ICP-MS zircon U–Pb age and geochemical characteristics of the Taohaotuoxiquan gabbro in northern Alxa, Inner Mongolia. *Geol. Bull. China* **2013**, *32*, 1536–1547. (In Chinese)
40. Winter, J. *Introduction to Igneous and Metamorphic Petrology*; Prentice Hall: Upper Saddle River, NJ, USA, 2001; p. 796.
41. Pearce, J.A.; Stern, R.J. The origin of back-arc basin magmas: Trace element and isotope perspectives. In *Back-Arc Spreading Systems: Geological, Biological, Chemical and Physical Interactions*; Christie, C.R., Lee, S.-M., Givens, S., Eds.; American Geophysical Union Geophysical Monograph; John Wiley & Sons, Inc.: Hoboken, NJ, USA, 2006; Volume 166, pp. 63–86.
42. Sun, S.S.; McDonough, W.F. Chemical and isotopic systematics of oceanic basalts: Implications for mantle composition and processes. In *Magmatism in the Ocean Basin*; Geological Society of London Special Publication: London, UK, 1989; Volume 42, pp. 313–345.
43. Marchesi, C.; Garrido, C.J.; Godard, M.; Proenza, J.A.; Gervilla, F.; Blanco-Moreno, J. Petrogenesis of highly depleted peridotites and gabbroic rocks from the Mayarí-Baracoa ophiolitic belt (eastern Cuba). *Contrib. Miner. Petrol.* **2006**, *151*, 717–736. [[CrossRef](#)]

44. Thirlwall, M.F.; Upton, B.G.J.; Jenkins, C. Interaction between continental lithosphere and the Iceland plume: Sr–Nd–Pb isotope chemistry of Tertiary basalts, NE Greenland. *J. Petrol.* **1994**, *35*, 839–897. [[CrossRef](#)]
45. Bogaard, P.F.J.; Wörner, G. Petrogenesis of basanitic to tholeiitic volcanic rocks from the Miocene Vogelsberg, Central Germany. *J. Petrol.* **2003**, *44*, 569–602. [[CrossRef](#)]
46. Saunders, A.D.; Storey, M.; Kent, R.W.; Norry, M.J. Consequences of plume-lithosphere interactions. In *Magmatism and the Causes of Continental Break-up*; Alabaster, T., Storey, B.C., Pankhurst, R.J., Eds.; Geological Society: London, UK, 1992; Volume 68, pp. 41–60.
47. Jung, C.; Jung, S.; Hoffer, E.; Berndt, J. Petrogenesis of tertiary mafic alkaline magmas in the Hoheifel, Germany. *J. Petrol.* **2006**, *47*, 1637–1671. [[CrossRef](#)]
48. Wilson, M. *Igneous Petrogenesis*; Chapman and Hall: London, UK, 1989; p. 466.
49. Rogers, N.; Macdonald, R.; Fitton, J.G.; George, R.; Smith, M.; Barreiro, B. Two mantle plumes beneath the east African rift system: Sr, Nd and Pb isotope evidence from Kenya Rift basalts. *Earth Planet. Sci. Lett.* **2000**, *176*, 387–400. [[CrossRef](#)]
50. Rudnick, R.L.; Fountain, D.M. Nature and composition of the continental crust—A lower crustal perspective. *Rev. Geophys.* **1995**, *33*, 267–309. [[CrossRef](#)]
51. Weaver, S.D.; Seal, J.C.; Gibson, I.L. Trace element data relevant to the origin of trachytic and pantelleritic lavas in the East African Rift System. *Contrib. Mineral. Petrol.* **1971**, *36*, 181–194. [[CrossRef](#)]
52. Lippard, S.J. The petrology of phonolites from Kenyan rift. *Lithos* **1973**, *6*, 217–234. [[CrossRef](#)]
53. Dai, J.G.; Wang, C.S.; Hebert, R.; Li, Y.L.; Zhong, H.T.; Guillaume, R.; Bezar, R.; Wei, Y.S. Late Devonian OIB alkaline gabbro in the YarlungZangbo suture zone: Remnants of the paleo-Tethys. *Gondwana Res.* **2011**, *19*, 232–243. [[CrossRef](#)]
54. Rudnick, R.; Gao, S. Composition of the continental crust. In *Treatise on Geochemistry*; Rudnick, R., Ed.; Elsevier-Pergamon: Oxford, UK, 2003; Volume 3, pp. 1–64.
55. Pearce, J.A. Geochemical fingerprinting of oceanic basalts with applications to ophiolite classification and the search for Archean oceanic crust. *Lithos* **2008**, *100*, 14–48. [[CrossRef](#)]
56. Zindler, A.; Hart, S. Chemical geodynamics. *Annu. Rev. Earth Planet. Sci.* **1986**, *14*, 493–571. [[CrossRef](#)]
57. Hart, S.R.; Hauri, E.H.; Oschmann, L.A.; Whitehead, J. Mantle plumes and entrainment: Isotopic evidence. *Science* **1992**, *256*, 517–520. [[CrossRef](#)]
58. Jahn, B.M.; Wu, F.Y.; Lo, C.H.; Tsai, C.H. Crust-mantle interaction induced by deep subduction of the continental crust: Geochemical and Sr–Nd isotopic evidence from post-collisional mafic-ultramafic intrusions of the northern Dabie complex, central China. *Chem. Geol.* **1999**, *157*, 119–146. [[CrossRef](#)]
59. Stolz, A.J.; Jochum, K.P.; Hofmann, A.W. Fluid- and melt-related enrichment in the subarc mantle: Evidence from Nb/Ta variations in island-arc basalts. *Geology* **1996**, *24*, 587–590. [[CrossRef](#)]
60. Taylor, S.R.; McLennan, S.M. *The Continental Crust: Its Composition and Evolution*; Blackwell Scientific Publications: London, UK, 1985; p. 312.
61. Chung, S.L.; Wang, K.L.; Crawford, A.J.; Kamenetsky, V.S.; Chen, C.H.; Lan, C.Y.; Chen, C.H. High-Mg potassic rocks from Taiwan: Implications for the genesis of orogenic potassic lavas. *Lithos* **2001**, *59*, 153–170. [[CrossRef](#)]
62. Seghedi, I.; Downes, H.; Szakacs, A.; Mason, P.; Thirlwall, M.; Rosu, E.; Pecskey, Z.; Marton, E.; Panaiotu, C. Neogene–Quaternary magmatism and geodynamics in the Carpathian–Pannonian region: A synthesis. *Lithos* **2004**, *72*, 117–146. [[CrossRef](#)]
63. Labanieh, S.; Chauvel, C.; Germa, A.; Quidelleur, X. Martinique: A clear case for sediment melting and slab dehydration as a function of distance to the trench. *J. Petrol.* **2012**, *53*, 2441–2464. [[CrossRef](#)]
64. Woodhead, J.D.; Eggins, S.M.; Johnson, R.W. Magma genesis in the New Britain Island Arc: Further insights into melting and mass transfer processes. *J. Petrol.* **1998**, *39*, 1641–1668. [[CrossRef](#)]
65. Leat, P.T.; Pearce, J.A.; Barker, P.F.; Millar, I.L.; Barry, T.L.; Larter, R.D. Magmagenesis and mantle flow at a subducting slab edge: The South Sandwicharc-basin system. *Earth Planet. Sci. Lett.* **2004**, *227*, 17–35. [[CrossRef](#)]
66. Saccani, E. A new method of discriminating different types of post-Archean ophiolitic basalts and their tectonic significance using Th–Nb and Ce–Dy–Yb systematics. *Geosci. Front.* **2015**, *6*, 481–501. [[CrossRef](#)]
67. Jenner, G.A.; Dunning, G.R.; Malpas, J.; Brown, M.; Brace, T. Bay of Islands and Little Port complexes, revisited: Age, geochemical and isotopic evidence confirm supra-subduction zone origin. *Can. J. Earth Sci.* **1991**, *28*, 135–162. [[CrossRef](#)]

68. Wilde, S.A. Final amalgamation of the Central Asian Orogenic Belt in NE China: Paleo-Asian Ocean closure versus Paleo-Pacific plate subduction—A review of the evidence. *Tectonophysics* **2015**, *662*, 345–362. [[CrossRef](#)]
69. Luo, H.L.; Wu, T.R.; Zhao, L. Zircon SHRIMP U–Pb dating of Wuliangsitai A-type granite on the northern margin of the North China Plate and tectonic significance. *Acta Petrol. Sin.* **2009**, *25*, 515–526.
70. Liu, Q.; Zhao, G.C.; Han, Y.G.; Eizenhöfer, P.R.; Zhu, Y.L.; Hou, W.Z.; Zhang, X.R. Timing of the final closure of the Paleo-Asian Ocean in the Alxa Terrane: Constraints from geochronology and geochemistry of Late Carboniferous to Permian gabbros and diorites. *Lithos* **2017**, *274*, 19–30. [[CrossRef](#)]
71. Wood, D.A. The application of a Th–Hf–Ta diagram to problems of tectonomagmatic classification and to establishing the nature of crustal contamination of basaltic lavas of the British Tertiary volcanic province. *Earth Planet. Sci. Lett.* **1980**, *50*, 11–30. [[CrossRef](#)]



© 2019 by the authors. Licensee MDPI, Basel, Switzerland. This article is an open access article distributed under the terms and conditions of the Creative Commons Attribution (CC BY) license (<http://creativecommons.org/licenses/by/4.0/>).